Opto-Electronic Advances

ISSN 2096-4579 CN 51-1781/TN

Third-harmonic generation and imaging with resonant Si membrane metasurface

Ze Zheng, Lei Xu, Lujun Huang, Daria Smirnova, Khosro Zangeneh Kamali, Arman Yousefi, Fu Deng, Rocio Camacho-Morales, Cuifeng Ying, Andrey E. Miroshnichenko, Dragomir N. Neshev and Mohsen Rahmani

Citation: Zheng Z, Xu L, Huang LJ, Smirnova D, Kamali KZ et al. Third-harmonic generation and imaging with resonant Si membrane metasurface. *Opto-Electron Adv* **6**, 220174(2023).

https://doi.org/10.29026/oea.2023.220174

Received: 31 October 2022; Accepted: 6 March 2023; Published online: 10 May 2023

Related articles

Crosstalk-free achromatic full Stokes imaging polarimetry metasurface enabled by polarization-dependent phase optimization

Yaxin Zhang, Mingbo Pu, Jinjin Jin, Xinjian Lu, Yinghui Guo, Jixiang Cai, Fei Zhang, Yingli Ha, Qiong He, Mingfeng Xu, Xiong Li, Xiaoliang Ma, Xiangang Luo

Opto-Electronic Advances 2022 **5**, 220058 doi: 10.29026/oea.2022.220058

Intelligent metaphotonics empowered by machine learning

Sergey Krasikov, Aaron Tranter, Andrey Bogdanov, Yuri Kivshar

Opto-Electronic Advances 2022 **5**, 210147 doi: 10.29026/oea.2022.210147

Graphene-empowered dynamic metasurfaces and metadevices

Chao Zeng, Hua Lu, Dong Mao, Yueqing Du, He Hua, Wei Zhao, Jianlin Zhao

Opto-Electronic Advances 2022 **5**, 200098 doi: 10.29026/oea.2022.200098

Quantum photonics based on metasurfaces

Jun Liu, Mingqian Shi, Zhuo Chen, Shuming Wang, Zhenlin Wang, Shining Zhu

Opto-Electronic Advances 2021 **4**, 200092 doi: 10.29026/oea.2021.200092

More related article in Opto-Electron Journals Group website

OEA Opto-Electronic Advances

http://www.oejournal.org/oea

OE_Journal @OptoElectronAdv

Opto-Electronic Advances

Article

August 2023, Vol. 6, No. 8

DOI: 10.29026/oea.2023.220174

Third-harmonic generation and imaging with resonant Si membrane metasurface

Ze Zheng[1], Lei Xu[1*], Lujun Huang[2,3], Daria Smirnova[4], Khosro Zangeneh Kamali[4], Arman Yousefi[1], Fu Deng[5], Rocio Camacho-Morales[4], Cuifeng Ying[1], Andrey E. Miroshnichenko[2], Dragomir N. Neshev[4] and Mohsen Rahmani[1*]

Dielectric metasurfaces play an increasingly important role in enhancing optical nonlinear generations owing to their ability to support strong light-matter interactions based on Mie-type multipolar resonances. Compared to metasurfaces composed of the periodic arrangement of nanoparticles, inverse, so-called, membrane metasurfaces offer unique possibilities for supporting multipolar resonances, while maintaining small unit cell size, large mode volume and high field enhancement for enhancing nonlinear frequency conversion. Here, we theoretically and experimentally investigate the formation of bound states in the continuum (BICs) from silicon dimer-hole membrane metasurfaces. We demonstrate that our BIC-formed resonance features a strong and tailorable electric near-field confinement inside the silicon membrane films. Furthermore, we show that by tuning the gap between the holes, one can open a leaky channel to transform these regular BICs into quasi-BICs, which can be excited directly under normal plane wave incidence. To prove the capabilities of such metasurfaces, we demonstrate the conversion of an infrared image to the visible range, based on the Third-harmonic generation (THG) process with the resonant membrane metasurfaces. Our results suggest a new paradigm for realising efficient nonlinear photonics metadevices and hold promise for extending the applications of nonlinear structuring surfaces to new types of all-optical near-infrared imaging technologies.

Keywords: nonlinear imaging; third-harmonic generation; bound states in the continuum; membrane metasurfaces

Zheng Z, Xu L, Huang LJ, Smirnova D, Kamali KZ et al. Third-harmonic generation and imaging with resonant Si membrane metasurface. *Opto-Electron Adv* **6**, 220174 (2023).

Introduction

In recent years, the field of nonlinear nanophotonics has grown enormously and attracted tremendous attention due to a vast range of related applications, including ultrasensitive sensing[1–3], optical microscopy[4–6], quantum metasurfaces and entangled photon pairs generation[7–12]. Contributed by the development of the growth and nano-fabrication of nonlinear materials, metasurfaces have become a flexible and versatile platform for the nonlinear generations at the nanoscale[13–16]. By utilising

[1]Advanced Optics and Photonics Laboratory, Department of Engineering, School of Science & Technology, Nottingham Trent University, Nottingham NG11 8NS, UK; [2]School of Engineering and Information Technology, University of New South Wales, Canberra ACT 2600, Australia; [3]School of Physics and Electronic Science, East China Normal University, Shanghai 200241, China; [4]ARC Centre of Excellence for Transformative Meta-Optical Systems (TMOS), Research School of Physics, Australian National University, Canberra ACT 2601, Australia; [5]Department of Physics, Hong Kong University of Science and Technology, Kowloon, Hong Kong SAR 999077, China.

*Correspondence: L Xu, E-mail: lei.xu@ntu.ac.uk; M Rahmani, E-mail: mohsen.rahmani@ntu.ac.uk

Received: 31 October 2022; Accepted: 6 March 2023; Published online: 10 May 2023

Open Access This article is licensed under a Creative Commons Attribution 4.0 International License.
To view a copy of this license, visit http://creativecommons.org/licenses/by/4.0/.

© The Author(s) 2023. Published by Institute of Optics and Electronics, Chinese Academy of Sciences.

the strong light-matter interaction within the sub-wavelength resonators, the effective nonlinearities can be significantly amplified in the nonlinear metasurfaces, as compared to their bulk counterparts[17]. Particularly, the optical performance of the metasurfaces can be effectively controlled via the domination of symmetry and parametric tuning[18–21]. Furthermore, metasurfaces made of dielectrics and semiconductors such as silicon and germanium, have been considered a promising platform for confining and manipulating light at the nanoscale based on the optically induced multipolar resonant effects[22,23]. Nowadays, the conception of enhanced nonlinear generations at the nanoscale has been theoretically demonstrated and experimentally achieved in various nonlinear processes, including second-harmonic generation (SHG), third-harmonic generation (THG), four-wave mixing (FWM), based on resonant dielectric metasurfaces, such as AlGaAs, GaAs, $LiNbO_3$, and Si metasurfaces[24–33]. Extreme light confinement within the metasurfaces is a critical factor in achieving strong light-matter interactions and generating nonlinear signals with higher intensity under relatively low-power input light.

Bound states in the continuum (BICs) recently emerge as a novel approach to manipulating the light-matter interactions[34]. The conception of BICs originates from quantum mechanics, and has now been observed and applied in metasurfaces and nonlinear generations to produce controllable light confinement within the resonators[27,33,35–40]. The typical dielectric metasurfaces consist of subwavelength resonators where the light is strongly confined in the vicinity of the resonators. Over the past few years, membrane metasurfaces, consisting of a single layer of nonlinear material with an array of holes, have shown unique optical properties compared to the traditional dielectric metasurfaces composed of an array of nanoparticles[32,41–43]. For example, membrane metasurfaces can support the resonances and maintain the nonlinear efficiency with a smaller unit-cell size compared to other platforms, offering more unit cells in the same area. This property expands the practical use of membrane metasurfaces, particularly suggesting a promising approach for improving the spatial resolution in imaging field. Besides, guided modes are widely employed in membrane metasurfaces[38,44], which offer more options on manipulating the light-matter interaction, particularly in nonlinear nanophotonics.

Infrared (IR) imaging and spectroscopy based on nonlinear metasurfaces have been recognised as a potential substitute for commercial IR imaging detectors due to its superiority of being ultra-compact, containing fewer components for signal conversion[45,46]. Relevant works have been demonstrated based on the GaAs nanoantenna[46] and Si nanopillar[47]. What has been indicated is that improving the conversion efficiencies of nonlinear generations can facilitate the practical use of IR imaging[46].

Here, we propose the employment of silicon membrane metasurfaces for augmenting THG process. Our proposed membrane metasurfaces consist of dimer holes (see Fig. 1) and can support multiple symmetry-protected BICs. By tuning the gap between the two holes, the symmetry-protected BICs can be transformed into the quasi-BICs, resulting in a strong electromagnetic field confinement within the silicon membrane via plane-wave illumination. Supporting multipolar resonances and concurrently maintaining small unit sizes and high-mode volume for enhancing nonlinear frequency conversion is a unique advantage of membrane metasurfaces, as compared to regular particle-based metasurfaces. We reveal the formation mechanisms of the BICs by utilising the symmetry of the structure and the multipolar model. We experimentally demonstrate the conversion of near-infrared image into visible based on the THG process in membrane metasurfaces. The exploitation of membrane metasurfaces in the nonlinear generation and its closely related application, infrared imaging, can contribute to the development of the light conversion nano-device and extend its applications, particularly the infrared imaging.

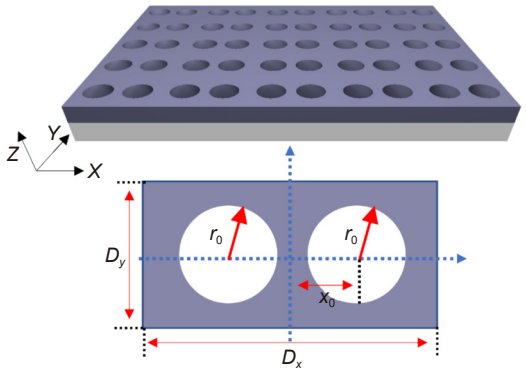

Fig. 1 | Schematic representation of the designed silicon membrane metasurface. The radius of the hole r_0 is set as 100 nm. The period along x and y directions D_x and D_y are set as 600 nm and 300 nm, respectively. The offset x_0 as the tunable factor is changed from 120 nm to 150 nm.

Results and discussion

Design and analysis

We consider an amorphous silicon (a-Si) membrane metasurfaces consisting of a silicon slab with dimer airy holes arranged periodically on a glass substrate, as schematically shown in Fig. 1. The radius of the hole is fixed as r_0=100 nm. We define the offset parameter x_0 as the distance from the center of one hole to the midline of the unit (with dimer hole) along the x direction. The period along x and y directions D_x and D_y are set to be 600 nm and 300 nm, respectively. Thus, when the offset x_0=150 nm, the dimer-hole membrane metasurfaces will be the same as a hole membrane metasurfaces with the unit cell period D_x=D_y=300 nm. The system of the a-Si membrane metasurfaces is invariant under the 180-degree rotation around the z-axis, which is defined as the operation C_2^z in this paper.

We first characterise the mode properties of such membrane metasurfaces by calculating the band structure based on the Massachusetts Institute of Technology Photonic-Bands (MPB) open sources[48]. Figure 2(a) shows the calculated band structure for the metasurfaces when x_0=150 nm. Here, based on modified Fabry-Perot model, we define the transverse electric modes as TE(l, m, n), where l, m, n are the quantum numbers of the mode along x, y, and z axes. Specifically, the total phase accumulation is a round trip is, π(l−1), π(m−1), and π(n−1), respectively. For the considered unit cell with pitch sizes of D_x=600 nm and D_y=300 nm, we observe two typical odd modes under C_2^z, TE(3, 1, 1) and TE(3, 1, 2) with their electric pattern M1 and M2 (see Fig. 2(b)). However, when x_0=150 nm, the pitch sizes (D_x × D_y) of unit cell changes from 600 × 300 nm to 300 × 300 nm. With the transformation of the unit cell, the two modes, TE(3, 1, 1) and TE(3, 1, 2), become even under C_2^z, decoupling to the odd leaky channel to the far-field. The features of TE(3, 1, 1) and TE(3, 1, 2) indicate that they are symmetry-protected BICs with infinite Q-factor when x_0=150 nm, and can be converted into quasi-BICs with finite Q-factor when we tune the offset x_0. Meanwhile, we characterise the mode properties of silicon disk metasurfaces based on the same mode TE(3, 1, 1), which is demonstrated in Supplementary information S1. The results prove that, as compared to disk metasurfaces, membrane metasurfaces provide a powerful platform for enhancing light-matter interactions with a smaller unit cell size.

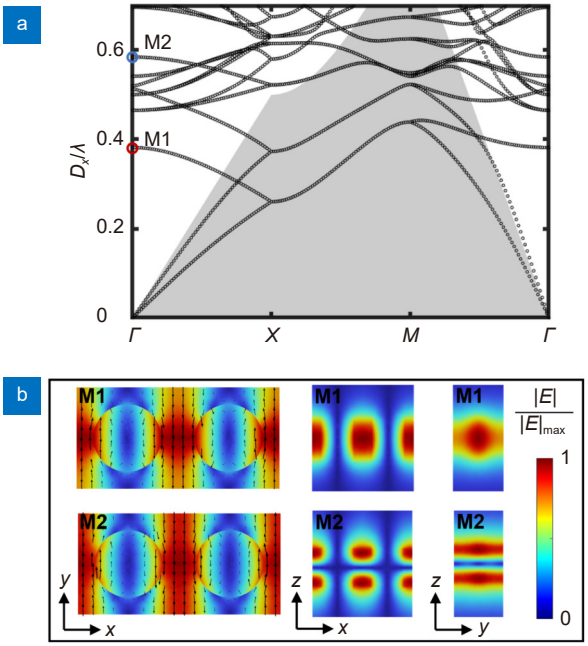

Fig. 2 | (**a**) Calculated bandgap structure for the metasurface with the positions of M1 (red circle) and M2 (blue circle) shown in the figure. (**b**) Near-field electric distributions for the mode TE(3, 1, 1) and TE(3, 1, 2).

By controlling the offset x_0, one can transform such an ideal BIC into a quasi-BIC. This phenomenon has been explained from the view of symmetry. This explanation is intuitive and concise to summarise the formation of the BIC, but hardly shows the process of the energy exchange from the bound modes to the external modes. Taking Mode 1 as an example, we then investigate and characterise the modes via spherical and Cartesian multipolar analysis. This enables us to observe it from the view of multipolar transformations, manifesting itself as a Fano feature in the optical response spectrum.

We perform the spherical and Cartesian multipolar analysis[49–51] for three different cases: x_0=120 nm, 135 nm and 150 nm, respectively. Please note that the ED, MD, EQ, MQ, EO, MO, p_y, and TD respectively represent the electric dipole (ED) and magnetic dipole (MD), electric quadrupole (EQ) and magnetic quadrupole (MQ), electric octupole (EO) and magnetic octupole (MO), the electric dipole moment along the y-axis (p_y), and electric Toroidal moment (TD). As can be seen in Fig. 3, TE(3, 1, 1) is dominated by ED excitation with a small contribution from the MQ and MO. The TD, MQ and MO do not contribute to the far-field radiation along the z direction due to zero overlap with the outgoing waves. The electric dipole moment along the y-axis p_y here plays a role in opening a leaky channel and transforming this

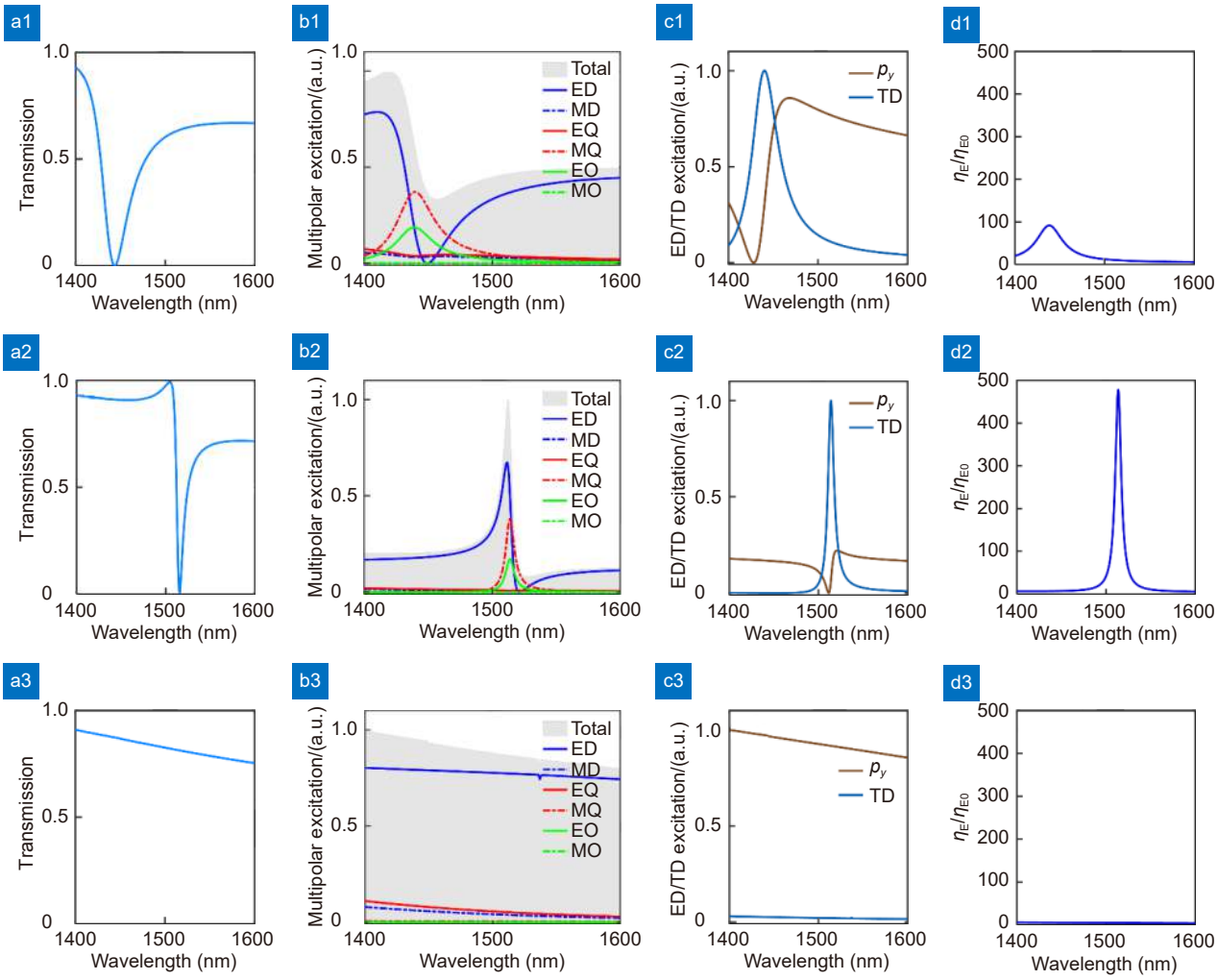

Fig. 3 | Calculated linear transmission spectra (**a1–a3**), spherical (**b1–b3**), Cartesian multipolar structures (**c1–c3**) and electric energy enhancement (**d1–d3**) inside the silicon film for the case when the offset is 120 (a1–d1), 135 (a2–d2) and 150 (a3–d3), respectively. In the spherical multipolar expansion, the ED, MD, EQ, MQ, EO, MO respectively represent the electric dipole (ED) and magnetic dipole (MD), electric quadrupole (EQ) and magnetic quadrupole (MQ), electric octupole (EO) and magnetic octupole (MO). In the Cartesian multipolar expansion, the p_y and TD represent the electric dipole moment along the *y*-axis (p_y) and electric Toroidal moment (TD).

ideal BIC into a quasi-BIC with a finite Q-factor.

By controlling the offset x_0, we can control the excitation and the coupling between the bright mode p_y and the dark mode TD, and thus control the energy exchange of the BIC with the external radiation channels, and the radiation damping rate at the resonance. When the offset increases from x_0=120 nm to x_0=135 nm, the radiation damping rate and the width of the resonance decrease significantly. The radiation has decreased accordingly as the excitation of the bright mode p_y decreases, as illustrated in Fig. 3(c1, c2). This corresponds to a significant enhancement of the electric energy density inside the silicon film, as demonstrated in Fig. 3(d1, d2). When the offset x_0=150 nm, it corresponds to an ideal BIC where the coupling with external plane-wave under normal incidence vanishes, as revealed in Fig. 3(a3–d3). From the multipolar structure, no TD excitation is observed, and the electric energy density inside the silicon film is negligible as compared to the two cases with x_0=120 nm and x_0=135 nm when a quasi-BIC is obtained. Figure 3 shows the process of how the leakage between the radiative channel and bound state vanishes (from x_0=120 nm to x_0=150 nm).

Fabrication and characterisation

We fabricated our sample using the standard electron beam lithography (EBL). First 235 nm amorphous silicon was deposited on a glass substrate via plasma-enhanced chemical vapor deposition (PECVD). It was followed by EBL on a positive resist, called ZEP, which was

used as a mask for inductively coupled plasma etching (ICP). Finally, the residual ZEP resist was removed from the surface. Figure 4(a) demonstrates the scanning electron microscopy (SEM) images of the fabricated metasurfaces sample, showing the top view and the side view (40-degree tilt). We measured and simulated the linear transmission spectrum of the metasurfaces under a white light source illumination (see Fig. 4(b, c)). Two pronounced asymmetric Fano line shapes are observed around λ= 980 nm and λ = 1510 nm, respectively. This indicates the excitation of the two quasi-BICs. The measured widths of the two states are around 50 nm and 20 nm, respectively.

We then measured the transmission spectra of our fabricated metasurfaces with different offsets, as shown in Fig. 5. As can be seen, the width of the resonance narrows with increasing the offset from 120 nm to 150 nm. This corresponds to the decrease in geometric asymmetry. The Fano feature in the spectrum vanishes when x_0=150 nm, corresponding to the inaccessibility of the ideal BIC supported by the metasurfaces. We also observe a slight redshift of the resonance while tuning the x_0 from 120 nm to 150 nm. Furthermore, we observed another Fano resonance at around the wavelength of 1000 nm. Similarly, it vanishes when x_0=150 nm. By performing the multipolar analysis, we conclude that this Fano resonance is mainly formed by the interference between the ED, EQ and MO resonances. (Multipolar structure and field distribution in Supplementary information S2)

We further investigate the angular dependence of the transmission spectrum by changing the incident angle θ, of the y-polarised pump light along xz plane, as shown in θ, the redshift of the two resonances has been observed. This matches well with the calculated band structure.

TH emission was measured under the normal incidence of a pump laser with different central wavelengths. A femtosecond laser beam with 150 fs pulse width and 80 MHz repetition rate was focused to a spot size of 21 μm at the sample position by an aspheric lens with a focal length of 5 cm. The pump polarisation was adjusted along the y axis to excite the designed BIC, and the wavelength was tuned, ranging from 1400 nm to 1600 nm. The mean power on the sample plane is around 21.2 mW, leading to a maximum peak intensity value of around 1.0 GW/cm^2. An objective with a numerical aperture (NA) of 0.4 was used to collect the transmitted TH emission in the forward direction, as demonstrated in Fig. 6(a). The experimentally measured TH signals from the metasurfaces with different offsets are shown in

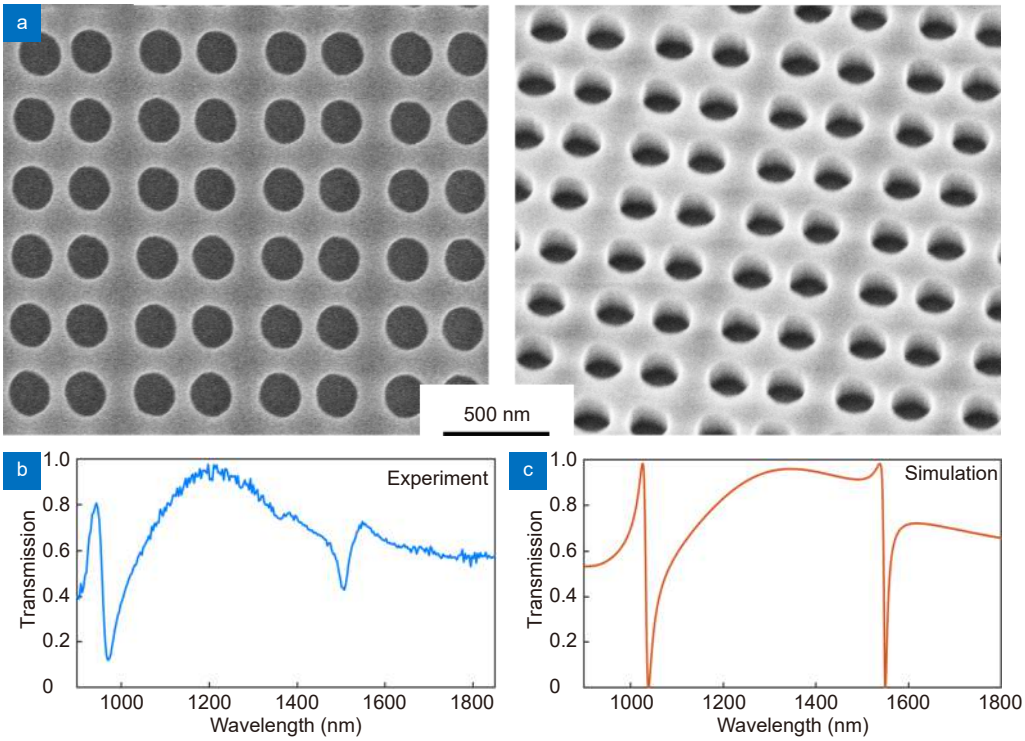

Fig. 4 | (**a**) SEM image of the fabricated sample. (**b**) The experimentally measured. (**c**) Simulated linear spectrum of the sample with offset being 135 nm.

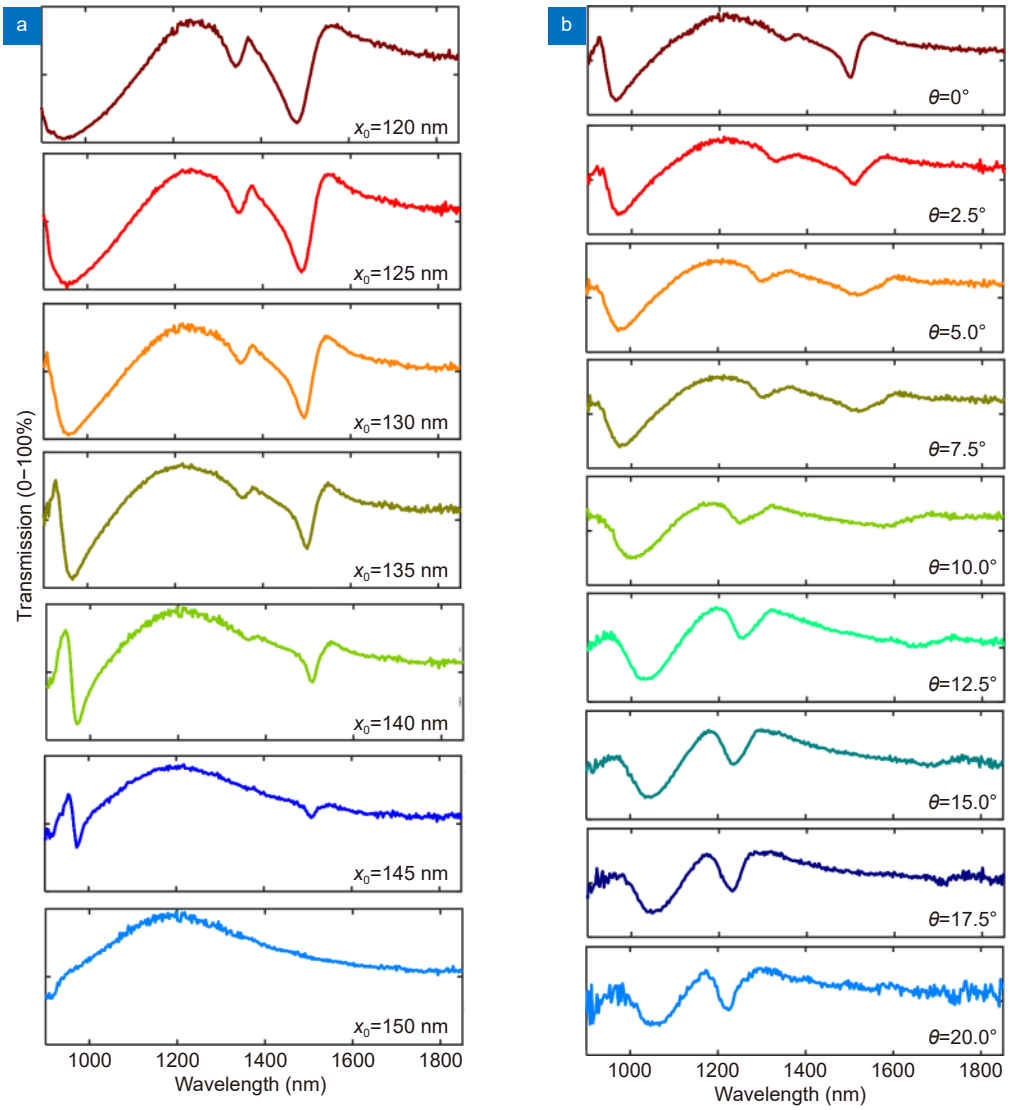

Fig. 5 | Measured linear spectra of metasurface samples with different offsets (**a**), and experimentally measured linear spectra of the metasurface samples with different incident angles of pump (**b**).

Fig. 6(b). The TH emissions are considerably enhanced at the resonance spectral position. With the offset increasing from 120 nm to 150 nm, the measured TH emission first increases to a maximum value when the offset is 135 nm, and then gradually decreases. As illustrated in Fig. 4, the width of the resonance is experimentally measured as 20 nm for x_0=135 nm, this matches well with the width of our pump laser around 1500 nm, suggesting the best coupling scheme for obtaining large nonlinear emission power[37]. With narrower resonances obtaining higher Q-factors when x_0=140 nm and x_0=145 nm, the nonlinear emission power decreases compared to x_0=135 nm. It shows that a resonance with a higher Q-factor wouldn't be beneficial under our experimental facilities. Thus, an optimised Q-factor that matches the experimentally available laser is desired for enhancing the nonlinear light-matter interaction process. When the offset is 150 nm, no significant enhancement of the TH emission is observed. This observation agrees with the fact that the ideal BIC is formed and the coupling of the BIC with external radiation has been suppressed when x_0=150 nm. The THG conversion efficiency is defined as the collected THG power divided by the incident pump power: $\eta_{\mathrm{THG}} = P_{\mathrm{THG}}/P_{\mathrm{input}}$. We obtained a maximum THG conversion efficiency of around 3.6×10^{-6} experimentally when the offset x_0=135 nm.

We further demonstrate the ability of THG imaging with the designed metasurfaces. Figure 7(a) shows the schematic of the THG imaging for demonstrating the ability of THG imaging by using the designed metasur-

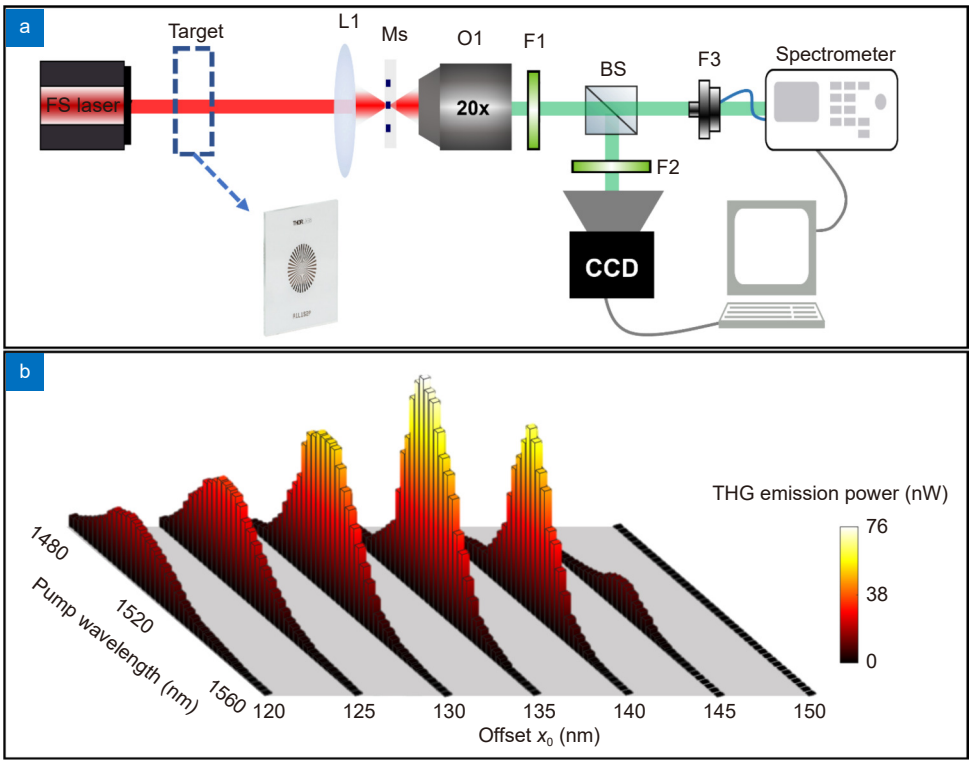

Fig. 6 | (**a**) The schematic of experimental setup for the THG imaging. The FS laser is the femtosecond laser. L1 is the aspheric lens that focus the beam into metasurfaces (MS). O1 is the 20× objective with *NA*=0.4. F1–F3 are the filters aiming to filter the near-infrared signal (F1) and control the intensity of the visible signal goes into the CCD camera (F2) and the spectrometer (F3). BS is the beam splitter. The target is imaged via the L1 to the plane, overlapping with the MS. The real image of the target and MS are imaged via the objective and then detected by the CCD camera (a CCD lens is included in the CCD camera). (**b**) The experimentally measured THG spectra of the samples with the different offset x_0.

faces. A NBS 1963A resolution test target is imaged by the focal lens onto the metasurfaces. Figure 7(b1–e1) show the visible image when the metasurfaces are overlapped with the target at different positions under a white light source illumination. We then overlap the metasurfaces sample (offset x_0=135 nm) with the image of the target near the focal plane, and illuminate the target with a 1512-nm IR laser. Figure 7(b2–e2) demonstrate the images captured by a scientific CCD camera (CS165MU/M, Thorlabs). As can be seen, the pattern of the overlapping area between the image of the target and the metasurfaces (see Fig. 7(b1–e1)) can be converted to visible images clearly (as demonstrated in Fig. 7(b2–e2)). Also, this is worth noting that the dimension of our stripes (around 6 μm width at the metasurfaces plane) is sufficient to cover an array of 10 × 10 units-cells. Therefore, the boundary effect on the field enhancement driven by the non-localised quasi-BICs is insignificant. As a result, the boundary effect is not expected to have much influence on the conversion efficiency[52,53]. Other strategies to bypass such an issue can be employing a hybrid metal-dielectric array to design high-quality modes inspired by symmetry-protected BIC mechanism[37,54]. As can be seen from Fig. 7(b2–e2), we have observed a strong nonlinear emission from the designed silicon metasurfaces area, as compared to the dark background (the silicon slab area) where no sizeable nonlinear emission is detected by our camera. Moreover, among current silicon metasurfaces, membrane metasurfaces can support THG from NIR to visible with a smaller unit-cell size (300×600 nm) (indicated in Supplementary information S3)[37,53,55,56]. It implies a better spatial resolution for imaging.

We successfully achieve the IR imaging with a clear multi-stripe pattern based on THG process. Such an approach suggests a novel platform for realising ultra-thin all-optical infrared imaging devices without the need of additional pump light. We believe that increasing the conversion efficiency of nonlinear generations based on the high-Q resonances and a large light-confined volume, such as employing light trapping assisted by slow light, increasing the spatial resolution based on small imaging units, carefully designing the optical setup to reduce the aberrations and fabricating the metasurfaces

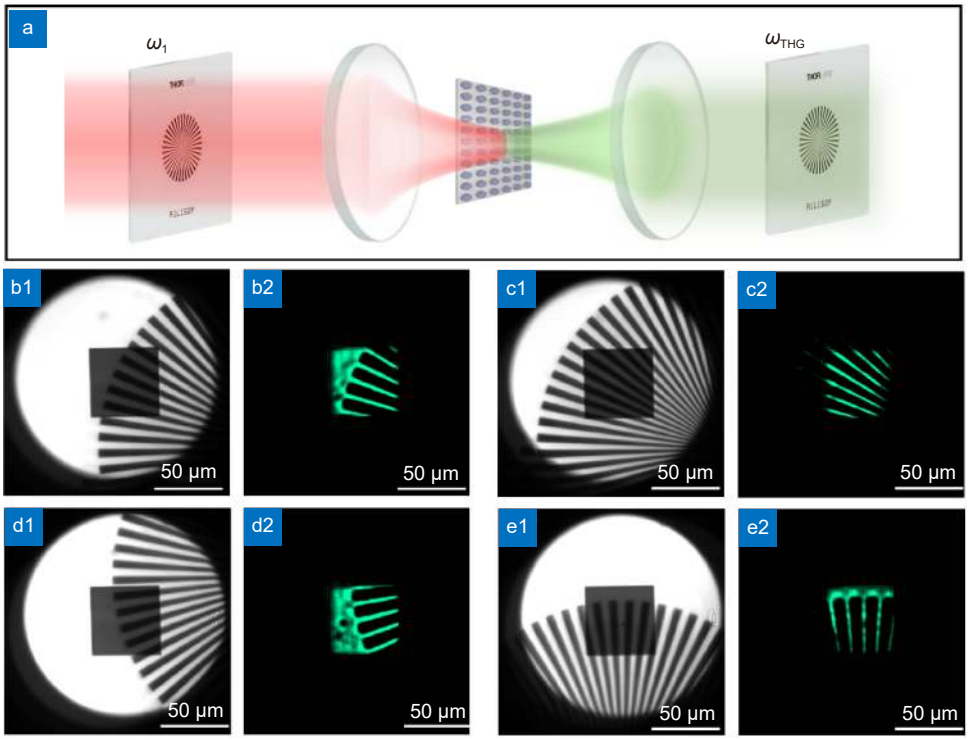

Fig. 7 | (**a**) The schematic of THG imaging based on Si membrane metasurfaces. The near-infrared signal passes through the target, then being converted into the visible signal via the metasurfaces, forming the target image on the CCD camera. (**b1**–**e1**) The images of the target and the metasurfaces under white light source illumination. (**b2**–**e2**) Transformed visible images of the target via membrane metasurfaces under NIR light illumination. Here the greenish colour has been used to indicate the nonlinear radiation spectrum position (504 nm). The patterns at three different positions of the target are converted to visible images clearly by the metasurfaces.

with larger areas can further improve the quality of IR imaging. In addition, compared to utilising the pump light to amplify the signal light in the SFG-based imaging, the THG-based imaging with only one input wavelength is more easily to be constructed in experiments. This simplicity may expand its application in sensing and infrared detecting.

Conclusions

In summary, we have demonstrated the potential of membrane metasurfaces for upconversion of an IR image to the visible wavelengths by the THG process based on Si material. Via tuning the offset x_0, we successfully convert the symmetry-protected BICs into quasi-BIC type resonances with infinite Q-factor. Furthermore, we reveal the formation mechanisms of those BICs from the views of symmetry and multipolar analysis. Meanwhile, after the test and characteristics of fabricated sample, we demonstrate infrared imaging as one of potential applications of enhanced THG based on Si membrane metasurfaces. The employment of membrane metasurfaces can further enhance the nonlinear generation in the aspect of offering a smaller unit size and a larger mode volume within the nonlinear material, which expands a range of applications, particularly all-optical infrared imaging at room temperature, and nonlinear spectroscopy.

References

1. Mesch M, Metzger B, Hentschel M, Giessen H. Nonlinear plasmonic sensing. *Nano Lett* **16**, 3155–3159 (2016).
2. Abarca A, Gómez-Sal P, Martín A, Mena M, Poblet JM et al. Ammonolysis of mono(pentamethylcyclopentadienyl) titanium(IV) derivatives. *Inorg Chem* **39**, 642–651 (2000).
3. Verma MS, Chandra M. Nonlinear plasmonic sensing for label-free and selective detection of mercury at picomolar level. *ACS Sens* **5**, 645–649 (2020).
4. Kravtsov V, Ulbricht R, Atkin JM, Raschke MB. Plasmonic nanofocused four-wave mixing for femtosecond near-field imaging. *Nat Nanotechnol* **11**, 459–464 (2016).
5. Deka G, Sun CK, Fujita K, Chu SW. Nonlinear plasmonic imaging techniques and their biological applications. *Nanophotonics* **6**, 31–49 (2017).
6. Frischwasser K, Cohen K, Kher-Alden J, Dolev S, Tsesses S et al. Real-time sub-wavelength imaging of surface waves with nonlinear near-field optical microscopy. *Nat Photonics* **15**, 442–448 (2021).
7. Wang K, Titchener JG, Kruk SS, Xu L, Chung HP et al. Quantum metasurface for multiphoton interference and state reconstruction. *Science* **361**, 1104–1108 (2018).
8. Stav T, Faerman A, Maguid E, Oren D, Kleiner V et al. Quantum

entanglement of the spin and orbital angular momentum of photons using metamaterials. *Science* **361**, 1101–1104 (2018).
9. Marino G, Solntsev AS, Xu L, Gili VF, Carletti L et al. Spontaneous photon-pair generation from a dielectric nanoantenna. *Optica* **6**, 1416–1422 (2019).
10. Santiago-Cruz T, Fedotova A, Sultanov V, Weissflog MA, Arslan D et al. Photon pairs from resonant metasurfaces. *Nano Lett* **21**, 4423–4429 (2021).
11. Parry M, Mazzanti A, Poddubny AN, Della Valle G, Neshev DN et al. Enhanced generation of nondegenerate photon pairs in nonlinear metasurfaces. *Advanced Photonics* **3**, 055001 (2021).
12. Liu J, Shi MQ, Chen Z, Wang SM, Wang ZL et al. Quantum photonics based on metasurfaces. *Opto-Electron Adv* **4**, 200092 (2021).
13. Li GX, Zhang S, Zentgraf T. Nonlinear photonic metasurfaces. *Nat Rev Mater* **2**, 17010 (2017).
14. Grinblat G. Nonlinear dielectric nanoantennas and metasurfaces: frequency conversion and wavefront control. *ACS Photonics* **8**, 3406–3432 (2021).
15. Gigli C, Leo G. All-dielectric $\chi^{(2)}$ metasurfaces: recent progress. *Opto-Electron Adv* **5**, 210093 (2022).
16. Fu R, Chen KX, Li ZL, Yu SH, Zheng GX. Metasurface-based nanoprinting: principle, design and advances. *Opto-Electron Sci* **1**, 220011 (2022).
17. Bonacina L, Brevet PF, Finazzi M, Celebrano M. Harmonic generation at the nanoscale. *J Appl Phys* **127**, 230901 (2020).
18. Gao XW, Hsu CW, Zhen B, Lin X, Joannopoulos JD et al. Formation mechanism of guided resonances and bound states in the continuum in photonic crystal slabs. *Sci Rep* **6**, 31908 (2016).
19. Jin JC, Lu J, Zhen B. Resonance-forbidden second-harmonic generation in nonlinear photonic crystals. *Nanophotonics* **10**, 4233–4239 (2021).
20. Huang LJ, Yu YL, Cao LY. General modal properties of optical resonances in subwavelength nonspherical dielectric structures. *Nano Lett* **13**, 3559–3565 (2013).
21. Huang LJ, Xu L, Rahmani M, Neshev DN, Miroshnichenko AE. Pushing the limit of high-*Q* mode of a single dielectric nanocavity. *Adv Photonics* **3**, 016004 (2021).
22. Smirnova D, Kivshar YS. Multipolar nonlinear nanophotonics. *Optica* **3**, 1241–1255 (2016).
23. Cui J H, Ma X L, Pu M B et al. Extraordinary strong optical rotation in weak chiral metasurface. *Opto-Electron Eng* **47**, 190052 (2020).
24. Lyu J, Rondepierre F, Jonin C, Brevet PF, Hamon C et al. Shape-controlled second-harmonic scattering from gold nanotetrapods. *J Phys Chem C* **126**, 9831–9835 (2022).
25. Celebrano M, Rocco D, Gandolfi M, Zilli A, Rusconi F et al. Optical tuning of dielectric nanoantennas for thermo-optically reconfigurable nonlinear metasurfaces. *Opt Lett* **46**, 2453–2456 (2021).
26. Carletti L, Zilli A, Moia F, Toma A, Finazzi M et al. Steering and encoding the polarization of the second harmonic in the visible with a monolithic $LiNbO_3$ metasurface. *ACS Photonics* **8**, 731–737 (2021).
27. Vabishchevich PP, Liu S, Sinclair MB, Keeler GA, Peake GM et al. Enhanced second-harmonic generation using broken symmetry III–V semiconductor fano metasurfaces. *ACS Photonics* **5**, 1685–1690 (2018).
28. Löchner FJF, Fedotova AN, Liu S, Keeler GA, Peake GM et al. Polarization-dependent second harmonic diffraction from resonant GaAs metasurfaces. *ACS Photonics* **5**, 1786–1793 (2018).
29. Liu S, Sinclair MB, Saravi S, Keeler GA, Yang YM et al. Resonantly enhanced second-harmonic generation using III–V semiconductor all-dielectric metasurfaces. *Nano Lett* **16**, 5426–5432 (2016).
30. Okhlopkov KI, Zilli A, Tognazzi A, Rocco D, Fagiani L et al. Tailoring third-harmonic diffraction efficiency by hybrid modes in high-Q metasurfaces. *Nano Lett* **21**, 10438–10445 (2021).
31. Gandolfi M, Tognazzi A, Rocco D, De Angelis C, Carletti L. Near-unity third-harmonic circular dichroism driven by a quasi-bound state in the continuum in asymmetric silicon metasurfaces. *Phys Rev A* **104**, 023524 (2021).
32. Xu L, Smirnova DA, Camacho-Morales R, Aoni RA, Kamali KZ et al. Enhanced four-wave mixing from multi-resonant silicon dimer-hole membrane metasurfaces. *New J Phys* **24**, 035002 (2022).
33. Carletti L, Kruk SS, Bogdanov AA, De Angelis C, Kivshar Y. High-harmonic generation at the nanoscale boosted by bound states in the continuum. *Phys Rev Res* **1**, 023016 (2019).
34. Hsu CW, Zhen B, Stone AD, Joannopoulos JD, Soljačić M. Bound states in the continuum. *Nat Rev Mater* **1**, 16048 (2016).
35. Anthur AP, Zhang HZ, Paniagua-Dominguez R, Kalashnikov DA, Ha ST et al. Continuous wave second harmonic generation enabled by quasi-bound-states in the continuum on gallium phosphide metasurfaces. *Nano Lett* **20**, 8745–8751 (2020).
36. Koshelev K, Tang YT, Li KF, Choi DY, Li GX et al. Nonlinear metasurfaces governed by bound states in the continuum. *ACS Photonics* **6**, 1639–1644 (2019).
37. Xu L, Zangeneh Kamali K, Huang LJ, Rahmani M, Smirnov A et al. Dynamic nonlinear image tuning through magnetic dipole quasi-BIC ultrathin resonators. *Adv Sci* **6**, 1802119 (2019).
38. Hsu CW, Zhen B, Lee J, Chua SL, Johnson SG et al. Observation of trapped light within the radiation continuum. *Nature* **499**, 188–191 (2013).
39. Yin XF, Jin JC, Soljačić M, Peng C, Zhen B. Observation of topologically enabled unidirectional guided resonances. *Nature* **580**, 467–471 (2020).
40. Hong PL, Xu L, Rahmani M. Dual bound states in the continuum enhanced second harmonic generation with transition metal dichalcogenides monolayer. *Opto-Electron Adv* **5**, 200097 (2022).
41. Yang QL, Liu MK, Kruk S, Xu YH, Srivastava YK et al. Polarization-sensitive dielectric membrane metasurfaces. *Adv Opt Mater* **8**, 2000555 (2020).
42. Yang QL, Kruk S, Xu YH, Wang QW, Srivastava YK et al. Mie-resonant membrane huygens' metasurfaces. *Adv Funct Mater* **30**, 1906851 (2020).
43. Tognazzi A, Rocco D, Gandolfi M, Locatelli A, Carletti L et al. High quality factor silicon membrane metasurface for intensity-based refractive index sensing. *Optics* **2**, 193–199 (2021).
44. Jin JC, Yin XF, Ni LF, Soljačić M, Zhen B et al. Topologically enabled ultrahigh-*Q* guided resonances robust to out-of-plane scattering. *Nature* **574**, 501–504 (2019).
45. Burns PN, Simpson DH, Averkiou MA. Nonlinear imaging. *Ultrasound Med Biol* **26**, S19–S22 (2000).
46. Del Rocio Camacho-Morales M, Rocco D, Xu L, Gili VF, Dimitrov N et al. Infrared upconversion imaging in nonlinear metasurfaces. *Adv Photonics* **3**, 036002 (2021).
47. Schlickriede C, Kruk SS, Wang L, Sain B, Kivshar Y et al. Nonlinear imaging with all-dielectric metasurfaces. *Nano Lett* **20**,

4370–4376 (2020).
48. Johnson SG, Joannopoulos JD. Block-iterative frequency-domain methods for Maxwell's equations in a planewave basis. *Opt Express* **8**, 173–190 (2001).
49. He Y, Guo GT, Feng TH, Xu Y, Miroshnichenko AE. Toroidal dipole bound states in the continuum. *Phys Rev B* **98**, 161112 (2018).
50. Gurvitz EA, Ladutenko KS, Dergachev PA, Evlyukhin AB, Miroshnichenko AE et al. The high-order toroidal moments and anapole states in all-dielectric photonics. *Laser Photonics Rev* **13**, 1800266 (2019).
51. Grahn P, Shevchenko A, Kaivola M. Electromagnetic multipole theory for optical nanomaterials. *New J Phys* **14**, 093033 (2012).
52. Campione S, Liu S, Basilio LI, Warne LK, Langston WL et al. Broken symmetry dielectric resonators for high quality factor Fano Metasurfaces. *ACS Photonics* **3**, 2362–2367 (2016).
53. Liu ZJ, Xu Y, Lin Y, Xiang J, Feng TH et al. High-*Q* quasibound states in the continuum for nonlinear metasurfaces. *Phys Rev Lett* **123**, 253901 (2019).
54. Volkovskaya I, Xu L, Huang LJ, Smirnov AI, Miroshnichenko AE et al. Multipolar second-harmonic generation from high-*Q* quasi-BIC states in subwavelength resonators. *Nanophotonics* **9**, 3953–3963 (2020).
55. Shcherbakov MR, Neshev DN, Hopkins B, Shorokhov AS, Staude I et al. Enhanced third-harmonic generation in silicon nanoparticles driven by magnetic response. *Nano Lett* **14**, 6488–6492 (2014).
56. Yang YM, Wang WY, Boulesbaa A, Kravchenko II, Briggs DP et al. Nonlinear Fano-resonant dielectric metasurfaces. *Nano Lett* **15**, 7388–7393 (2015).

Acknowledgements

Z. Zheng acknowledges the support from the Royal Society scholarship. L. Xu and M. Rahmani acknowledge support from the UK Research and Innovation Future Leaders Fellowship (MR/T040513/1). The authors acknowledge the use of NTU High Performance Computing cluster Hamilton, and the Australian National Fabrication Facility (ANFF), the ACT Node.

Author contributions

All authors commented on the manuscript.

Competing interests

The authors declare no competing financial interests.

Supplementary information

Supplementary information is available for this paper at https://doi.org/10.29026/oea.2023.220174